

Optical properties of graphite from first-principles calculations

R. Ahuja

Condensed Matter Theory Group, Department of Physics, Uppsala University, Box 530 S-751 21, Uppsala, Sweden

S. Auluck

Department of Physics, University of Roorkee, Roorkee-247 667, India

J. M. Wills

Theoretical Division, Los Alamos National Laboratory, Los Alamos, New Mexico 87544

M. Alouani

Department of Physics, Ohio State University, Ohio

B. Johansson and O. Eriksson

Condensed Matter Theory Group, Department of Physics, Uppsala University, Box 530 S-751 21, Uppsala, Sweden

(Received 14 May 1996)

We present theoretical results for the frequency-dependent dielectric response, both for the electric field parallel and perpendicular to the c axis of graphite. The calculations are performed using a full-potential linear muffin-tin orbital method. Our calculations show fair agreement with experimental data and the different features observed are identified from interband transitions in various regions of the Brillouin zone. The anisotropy of the dielectric function is discussed in detail and shown to be due to the difference in the optical matrix elements for the two different polarizations, which is a result of the anisotropic crystallographic and electronic properties of graphite. [S0163-1829(97)03904-0]

I. INTRODUCTION

Graphite can be regarded as an archetype of layered crystals. Intraplanar sp^2 bonding leaves a singly occupied p orbital at each C atomic site, and intraplanar π orbitals are formed from these p states, causing the semimetallic character of the solid. The weak interplanar interaction is well known, giving graphite its utility as a lubricant. Two polymorphic forms of graphite are common: the hexagonal and rhombohedral form. Hexagonal graphite (which we focus on here) has an abnormally large c/a ratio ($c/a=2.7259$). This gives rise to a large anisotropy in the structural and electronic properties. The carbon atoms in the basal plane are bound together by strong covalent bonds (σ), whereas the binding between the adjacent planes is weak and caused by van der Waals bonds. As a result the interlayer nearest-neighbor distance between the atoms (3.35 \AA) is much larger than the in-plane nearest-neighbor distance (1.42 \AA). This rather unique formation of σ and π orbitals in graphite also strongly influences the optical properties, as we shall demonstrate below.

There are many measurements of the structural and electronic properties of hexagonal graphite. The physical properties of graphite have been extensively studied through Raman scattering,¹⁻⁴ infrared reflectance,^{2,5-7} inelastic neutron scattering,⁸ elastic constant measurements,⁹ angle-resolved photoemission,¹⁰⁻¹³ and inverse photoemission¹³⁻¹⁸ experiments. It has been established that in general the results of various experiments are in agreement with energy band-structure calculations at ambient pressure (see below).

The energy band structure of graphite in an energy range

close to the Fermi energy (E_F) was first calculated by McClure¹⁹ and Slonczewski and Weins²⁰ (commonly known as the SWMcC model) using the $\mathbf{k}\cdot\mathbf{p}$ method. In this model the energy eigenvalues near E_F are given in terms of seven parameters that define the interaction energies between the orbitals from different carbon atoms within the basal plane and carbon atoms in the neighboring planes. The electronic structure of graphite has also been calculated self-consistently by means of the local density approximation (LDA), using different computational methods such as the linear combination of atomic orbitals method,²¹ the Korringa-Kohn-Rostoker method,²² the full-potential linearized augmented plane wave (FPLAPW) method,^{23,24} the pseudopotential method,²⁵⁻²⁷ and the full-potential linear muffin-tin orbitals (FPLMTO) method.²⁸

There are also excellent optical²⁹⁻³² and Fermi surface data³³ available for graphite but most of the energy band calculations do not make any serious attempt to compare these data with theory. However, earlier, empirical band calculations did make this comparison and obtained relatively good results. Recently the present authors calculated the pressure dependence of the so-called A1 and A2 optical transitions (attributed to interband transitions occurring at the symmetry point K) and found good agreement with recent optical reflectivity data of Hanfland, Beister, and Syassen.⁴ However, to our knowledge no first-principles work on the frequency-dependent dielectric constants has been published for graphite. In the present work we report on such calculations and compare with available high-quality experimental data.²⁹ The present work also describes in some detail how, in our full-potential linear muffin-tin orbital method, we have

implemented the formalism describing the dielectric response. We thus report on self-consistent calculations of the frequency-dependent dielectric function (with the electric field vector of the light both parallel and perpendicular to the crystallographic c axis) of graphite at ambient pressure using a method that does not rely on approximations concerning the geometry of the calculated potential and that is based on so-called linear muffin-tin orbitals.³⁴

II. DETAILS OF CALCULATIONS

A. Generating the potential and eigenvalues

As mentioned, we have used an all-electron, FPLMTO technique.³⁴ In this method one makes use of the variational principle, thus expressing the crystal wave function as a linear combination of Bloch sums of so-called muffin-tin orbitals, which are centered on the atoms. Hence the wave function is written as

$$\Psi^{\mathbf{k}}(\mathbf{r}) = \sum_t c_t \sum_{\mathbf{R}} e^{i\mathbf{k}\cdot\mathbf{R}} \phi_t(\mathbf{r} - \mathbf{r} - \boldsymbol{\tau}_t), \quad (1)$$

where \mathbf{k} is the crystal momentum, \mathbf{R} a Bravais lattice vector, $\boldsymbol{\tau}_t$ an atomic site, ϕ_t a muffin-tin orbital, and t a common index for atomic type and the different quantum numbers characterizing the atomiclike basis functions. For instance, the index t includes the principle quantum number (n), angular momentum (ℓ), and magnetic quantum number (m). The basis functions are augmented linear muffin-tin orbitals.^{35,36} This basis is defined to be numerical, atomic-like, functions inside the muffin-tin spheres surrounding each atom of the lattice. Outside the spheres (in the interstitial) the basis functions are linear combinations of (atomic centered) Hankel or Neuman functions (so-called tails or envelope functions) with nonzero kinetic energy (κ^2). At the muffin-tin sphere boundary each basis function from inside is connected in a continuous and differentiable way to a tail outside, with a specific kinetic energy. We did not use a minimal basis set but instead a so-called double basis. Thus Eq. (1) involved sums over pairs of basis functions inside a muffin-tin sphere, with the two atomiclike functions in a given pair characterized by the same n , l , and m , but each connecting to a different tail with a unique kinetic energy, say κ_1^2 and κ_2^2 , respectively. Thus the index t in Eq. (1) includes also the kinetic energy of the tail functions used. Since calculations of interband transitions, which are involved in the optical spectra, require very accurate eigenvalues it is beneficial to be able to go beyond a minimal basis set. In the summation in Eq. (1) one normally includes basis functions that are the most important ones for describing the valence states. In graphite this means $2s$, $2p$, and possibly $3d$ basis functions. However, the accuracy of the calculated eigenvalues is also improved if one augments the traditional basis functions, mentioned above, with states that have a higher principle quantum number. In the case of graphite this means including also the $3s$ and $3p$ states. As a matter of fact we found it necessary to include also these states in order to obtain well converged wave functions and optical spectra. In previous work we have routinely used this technique for systems where low-lying pseudo core states had to be included in the basis. Note that this does not necessarily

mean that one performs a so-called two panel calculation, where different sets of states are treated separately from the others. In our present theory we include all states in one fully hybridizing basis set thus maintaining good variational freedom for all states considered. Next, from the Reyleigh-Ritz method we obtain a secular determinant, which, when it has been diagonalized (numerically), yields eigenvalues and for each eigenvalue, $\epsilon_{\mathbf{k}}$, a corresponding set of (optimized) coefficients, c_t , thus giving a best representation of the crystal wave function $\Psi^{\mathbf{k}}$.

In the generation of the potential and charge density the unrestricted shape was provided by an expansion of spherical harmonic functions (with the correct symmetry) inside the muffin-tin spheres and by a Fourier series in the interstitial region. The integration over the Brillouin zone was done using the special point sampling³⁷ with a Gaussian smearing of width 20 mRy and using 108 k points in 1/12th of the Brillouin zone. Moreover, the calculations were done at the experimental lattice constants. The exchange and correlation part of the potential was calculated using the LDA with the Hedin-Lundqvist³⁸ (HL) parametrization.

B. Calculating the dielectric functions

The ($q=0$) dielectric function was calculated in the momentum representation, which requires matrix elements of the momentum, \mathbf{p} , between occupied and unoccupied eigenstates. To be specific the imaginary part of the dielectric function, $\epsilon_2(\omega) \equiv \text{Im}\epsilon(\mathbf{q}=0, \omega)$, was calculated from³⁹

$$\epsilon_2^{ij}(\omega) = \frac{4\pi^2 e^2}{Vm^2\omega^2} \sum_{\mathbf{kn}'\sigma} \langle \mathbf{kn}\sigma | p_j | \mathbf{kn}'\sigma \rangle \langle \mathbf{kn}'\sigma | p_i | \mathbf{kn}\sigma \rangle \times f_{\mathbf{kn}}(1 - f_{\mathbf{kn}'}) \delta(e_{\mathbf{kn}'} - e_{\mathbf{kn}} - \hbar\omega). \quad (2)$$

In Eq. (2), e is the electron charge, m its mass, V the volume, and $f_{\mathbf{kn}}$ the Fermi distribution. Moreover, $|\mathbf{kn}\sigma\rangle$ is the crystal wave function corresponding to the n th eigenvalue with crystal momentum \mathbf{k} and spin σ . With our spherical wave basis functions, the matrix elements of the momentum operator are conveniently calculated in spherical coordinates and for this reason the momentum is written as $\mathbf{p} = \sum_{\mu} \mathbf{e}_{\mu}^* p_{\mu}$,⁴⁰ where μ is -1 , 0 , or 1 , $\mathbf{e}_{-1} = (1/\sqrt{2})(\mathbf{e}_x - i\mathbf{e}_y)$, $\mathbf{e}_0 = \mathbf{e}_z$, $\mathbf{e}_1 = (-1/\sqrt{2})(\mathbf{e}_x + i\mathbf{e}_y)$, and $p_{-1} = (1/\sqrt{2})(p_x - ip_y)$, $p_0 = p_z$, and $p_1 = (-1/\sqrt{2})(p_x + ip_y)$.⁴¹

The evaluation of the matrix elements in Eq. (2) is done over the muffin-tin region and the interstitial separately. The integration over the muffin-tin spheres is similar to that reported by Oppeneer *et al.*⁴² and Gasche³⁹ in their atomic sphere approximation calculations. In our theoretical method, a basis function $\phi_t^{\mathbf{k}}(\mathbf{r}) = \sum_{\mathbf{R}} e^{i\mathbf{k}\cdot\mathbf{R}} \phi_t(\mathbf{r} - \boldsymbol{\tau}_t - \mathbf{R})$ [see Eq. (1)] inside a muffin-tin sphere at $\boldsymbol{\tau}_t$ in the primitive cell is in a compact form expressed as

$$\phi_t^{\mathbf{k}}(\mathbf{r})|_{|\mathbf{r}-\boldsymbol{\tau}_t|<S_t} = \sum_L i^{\ell} Y_L(\mathbf{r}, \boldsymbol{\tau}_t) \mathbf{U}_{\ell}(e_t; r_t) \times \Omega_{\ell}(e_t, \kappa_t) \mathbf{T}_{\tau_t; \tau_t L}(\kappa_t, \mathbf{k}), \quad (3)$$

where the index L denotes the pair ℓm , $\mathbf{U}_{\ell}(e; r) = [\phi_{\ell}(e; r), \phi_{\ell}(e; r)]$ is a row vector containing the LMTO

radial basis functions [$\phi_{\ell}(e;r)$ is a numerical function evaluated at energy e using the spherical part of the potential inside the muffin-tin sphere and $\dot{\phi}_{\ell}(e;r)$ is the energy derivative of this function],³⁵ $\mathbf{T}_{\tau L;\tau' L'}(\boldsymbol{\kappa}, \mathbf{k}) = [\delta(\tau\tau')\delta(LL'), B_{\tau L;\tau' L'}(\boldsymbol{\kappa}, \mathbf{k})]^T$ is a column vector containing the structure constants \mathbf{B} , and $\boldsymbol{\Omega}_{\ell\tau}$ is a 2×2 matrix that matches \mathbf{U} continuously and differentiably to the vector of (scaled) spherical Bessel functions⁴³ [$K_{\ell}(\boldsymbol{\kappa}, S_{\tau}), J_{\ell}(\boldsymbol{\kappa}, S_{\tau})$] at the muffin-tin radius S_{τ} . The matrix $\boldsymbol{\Omega}_{\ell\tau}$ may be written as

$$\boldsymbol{\Omega}_{\ell\tau} = \begin{pmatrix} \Omega_1 & \Omega_2 \\ \Omega_3 & \Omega_4 \end{pmatrix}, \quad (4)$$

where $\Omega_1 = K_{\ell\tau}(\boldsymbol{\kappa}, S_{\tau})/\Phi_{\ell\tau}(D_K, S_{\tau})$, $\Omega_2 = J_{\ell\tau}(\boldsymbol{\kappa}, S_{\tau})/\Phi_{\ell\tau}(D_J, S_{\tau})$, $\Omega_3 = \omega_{\ell\tau}(D_K)K_{\ell\tau}(\boldsymbol{\kappa}, S_{\tau})/\Phi_{\ell\tau}(D_K, S_{\tau})$, and $\Omega_4 = \omega_{\ell\tau}(D_J)J_{\ell\tau}(\boldsymbol{\kappa}, S_{\tau})/\Phi_{\ell\tau}(D_J, S_{\tau})$. In the expressions above D_K and D_J are the values of the logarithmic derivative of the spherical Bessel functions at the muffin-tin sphere. Moreover, $\Phi_{\ell}(D, r) = \phi_{\ell}(e;r) + \omega(D)\dot{\phi}_{\ell}(e;r)$, where D is the value of the logarithmic derivative, $\omega(D) = -[\phi_{\ell}(e;r)/\dot{\phi}_{\ell}(e;r)](D - D_e)/(D - \dot{D}_e)$ and D_e and \dot{D}_e are the logarithmic derivatives of the functions $\phi_{\ell}(e;r)$ and $\dot{\phi}_{\ell}(e;r)$, respectively. Thus the wave function inside each muffin-tin sphere [Eq. (3)] may simply be written as a radial function times a spherical harmonic; $f(r)i^{\ell}Y_{\ell m}(\hat{r})$.

Using this expression for the wave function inside the muffin-tin spheres, we calculate the matrix elements in Eq. (2) using

$$\begin{aligned} \mathbf{p}f(r)i^{\ell}Y_{\ell m}(\hat{r}) = & - \sum_{\mu} \tilde{e}_{\mu}^* \left[\mathcal{G}(\ell m; \ell - 1 m + \mu; 1 \mu) \left(\frac{d}{dr} + \frac{\ell + 1}{r} \right) f(r) i^{\ell-1} Y_{\ell-1 m + \mu}(\hat{r}) \right. \\ & \left. + \mathcal{G}(\ell m; \ell + 1 m + \mu; 1 \mu) \left(\frac{d}{dr} - \frac{\ell}{r} \right) f(r) i^{\ell+1} Y_{\ell+1 m + \mu}(\hat{r}) \right], \end{aligned} \quad (5)$$

where the coefficients \mathcal{G} are related to Gaunt coefficients:

$$\mathcal{G}(\ell_1 m_1; \ell_2 m_2; \ell_3 m_3) \equiv i^{\ell_1 - \ell_2 + \ell_3} \left(\frac{4\pi}{2\ell_3 + 1} \right)^{1/2} \int d\Omega Y_{\ell_1 m_1} Y_{\ell_2 m_2}^* Y_{\ell_3 m_3}. \quad (6)$$

In the interstitial, a basis function is expressed as

$$\phi_i^{\mathbf{k}}(\mathbf{r}) = \sum_{\mathbf{R}} e^{i\mathbf{k} \cdot \mathbf{R}} K_{\ell_i}(\boldsymbol{\kappa}_i, |\mathbf{r} - \boldsymbol{\tau}_i - \mathbf{R}|) i^{\ell_i} Y_{\ell_i}(\mathbf{r} - \boldsymbol{\tau}_i - \mathbf{R}). \quad (7)$$

Because the momentum operator commutes with the Laplacian, the matrix elements of momentum over the interstitial can be calculated as an integral over the surface of the muffin-tin spheres:

$$\begin{aligned} \int_{\Omega_i} d^3 r \phi_i^* \mathbf{p} \phi_j &= \frac{-1}{\kappa_j^2 - \kappa_i^2} \sum_{\mu} \mathbf{e}_{\mu}^* \int_{\Omega_i} d^3 r \nabla \cdot [\phi_i^* \nabla p_{\mu} \phi_j - (\nabla \phi_i)^* p_{\mu} \phi_j] \\ &= \frac{1}{\kappa_j^2 - \kappa_i^2} \sum_{\tau} S_{\tau}^2 \int_{|\mathbf{r} - \boldsymbol{\tau}| = S_{\tau}} d\Omega \left[\phi_i^* \frac{\partial}{\partial r} \mathbf{p} \phi_j - \left(\frac{\partial}{\partial r} \phi_i \right)^* \mathbf{p} \phi_j \right]. \end{aligned} \quad (8)$$

Analogous to Eq. (3), a basis function on the surface of a muffin-tin sphere at site τ is

$$\phi_i^{\mathbf{k}}(\mathbf{r})|_{|\mathbf{r} - \boldsymbol{\tau}| = S_{\tau}} = \sum_L i^{\ell} Y_L(\mathbf{r}_{\tau}) [K_{\ell}(\boldsymbol{\kappa}_i, S_{\tau}), J_{\ell}(\boldsymbol{\kappa}_i, S_{\tau})] \mathbf{T}_{\tau L; \tau_i L_i}(\boldsymbol{\kappa}_i, \mathbf{k}). \quad (9)$$

Analogous to Eq. (5), we calculate the surface integral, Eq. (8), using

$$\begin{aligned} \mathbf{p}[K_{\ell}(\boldsymbol{\kappa}, r), J_{\ell}(\boldsymbol{\kappa}, r)] i^{\ell} Y_{\ell m}(\hat{r}) &= \sum_{\mu} \mathbf{e}_{\mu}^* \{ -\mathcal{G}(\ell m; \ell - 1 m + \mu; 1 \mu) [\kappa^2 K_{\ell+1}(\boldsymbol{\kappa}, r), j_{\ell+1}(\boldsymbol{\kappa}, r)] i^{\ell-1} Y_{\ell-1 m + \mu}(\hat{r}) \\ &+ \mathcal{G}(\ell m; \ell + 1 m + \mu; 1 \mu) [K_{\ell+1}(\boldsymbol{\kappa}, r), \kappa^2 J_{\ell+1}(\boldsymbol{\kappa}, r)] i^{\ell+1} Y_{\ell+1 m + \mu}(\hat{r}) \}. \end{aligned} \quad (10)$$

TABLE I. Characteristic energy levels (in eV) at the Γ point for graphite relative to the Fermi energy using different basis sets.

	3(2s2p)	3(2s2p) 2(3s3p)	3(2s2p) 3(3s3p)	3(2s2p) 2(3d)	3(2s2p) 3(3d)	3(2s2p)2(3d) 3(3s3p)	3(2s2p)3(3d) 3(3s3p)	Experimental
Bottom σ	-19.55	-19.68	-19.32	-19.36	-19.46	-19.44	-19.44	-20.6
	-19.34	-19.37	-18.96	-19.15	-19.14	-19.14	-19.13	
Bottom π	-8.69	-8.70	-8.82	-8.57	-8.59	-8.58	-8.57	-8.1, ^a -8.5 ^b
	-6.66	-6.68	-6.54	-6.51	-6.52	-6.52	-6.51	-7.2, ^a -5.7, ^c -6.6 ^b
Top σ	-3.21	-3.21	-2.83	-2.93	-3.02	-3.04	-3.03	-4.6 ^a - 5.5 ^b
	-3.20	-3.20	-2.82	-2.92	-3.02	-3.04	-3.02	
	-3.19	-3.19	-2.81	-2.91	-3.00	-3.02	-3.01	
	-3.18	-3.18	-2.80	-2.91	-3.00	-3.02	-3.00	
Unoccupied σ^*	4.39	3.98	3.08	4.02	3.91	3.91	3.92	
	8.28	8.21	8.49	8.52	8.29	8.26	8.27	6.9 ^a
	8.28	8.22	8.50	8.52	8.29	8.27	8.27	
	8.33	8.26	8.56	8.58	8.35	8.31	8.32	
	8.34	8.26	8.57	8.58	8.35	8.32	8.33	

^aEberhardt *et al.* (Ref. 11).

^bLaw *et al.* (Ref. 12).

^cBianconi *et al.* (Ref. 44).

In the limit $\kappa_i^2 \rightarrow \kappa_j^2$ in Eq. (8), the difference $\kappa_j^2 \rightarrow \kappa_i^2$ is absorbed into κ^2 derivatives of the Bessel function vectors (K, J) and κ^2 derivatives of the structure functions in the vector T . Finally, by using the symmetrized momentum operator $\langle \psi_i | \vec{p} | \phi_j \rangle \equiv \frac{1}{2} (\langle \phi_i | \mathbf{p} \phi_j \rangle + \langle \mathbf{p} \phi_i | \phi_j \rangle)$, both muffin-tin and interstitial contributions to the matrix elements are separately Hermitian and are explicitly calculated as such.

The summation over the Brillouin zone in Eq. (2) is calculated using linear interpolation on a mesh of uniformly distributed points, i.e., the tetrahedron method. Matrix elements, eigenvalues, and eigenvectors are calculated in the irreducible part of the Brillouin zone. The correct symmetry for the dielectric constant was obtained by averaging the calculated dielectric function. Finally, the real part of the dielectric function, $\epsilon_1(\omega)$, is obtained from $\epsilon_2(\omega)$ using the Kramers-Kronig transformation,

$$\epsilon_1(\omega) \equiv \text{Re}[\epsilon(\mathbf{q}=0, \omega)] \\ = 1 + \frac{1}{\pi} \int_0^\infty d\omega' \epsilon_2(\omega') \left(\frac{1}{\omega' - \omega} + \frac{1}{\omega' + \omega} \right). \quad (11)$$

In order to calculate ϵ_1 one needs to have a good representation of ϵ_2 up to high energies. In the present work we have calculated ϵ_2 up to 4 Ry above the Fermi level and this was the truncation energy in Eq. (11). A test that modified this energy cutoff showed that 4 Ry is accurate to give a reliable ϵ_1 function at lower energies.

III. RESULTS AND DISCUSSIONS

A. Electronic structure

Since the quality of the calculated optical spectra depends on the accuracy of the one electron energies and wave functions we discuss shortly the convergence of the eigenvalues with respect to basis set truncation. In Table I we thus compare the eigenvalues at the Γ point for seven different basis

sets. As is clear from the table, graphite is a very delicate material to study in that one needs a very large basis set to achieve convergence. For the calculation with the largest basis we can compare theory and the experimentally obtained eigenvalues at the Γ point. The agreement is typically within 1 eV, but one should bear in mind that density functional theory is designed to give a good ground-state total energy and may not necessarily give excited-state properties through the one-particle eigenvalues. In our previous work²⁸ a smaller basis set was used resulting in less accurate eigenvalues.

B. Optical spectra

In the discussion that follows we will refer to $\epsilon_2^{ij}(\omega)$ as $\epsilon_2^\perp(\omega)$ when $i=j=x$ and as $\epsilon_2^\parallel(\omega)$ when $i=j=z$. The same notation will be used for $\epsilon_1^{ij}(\omega)$. In Fig. 1 we compare theory with experiment for the imaginary part of the perpendicular dielectric function, $\epsilon_2^\perp(\omega)$, and in Fig. 2 we make the corresponding comparison for the parallel dielectric function, $\epsilon_2^\parallel(\omega)$. The experimental data in Figs. 1 and 2 are from Daniels *et al.*²⁹ Before comparing experiment and theory in detail we note that we have not included a Drude term in the theoretical curves. The Drude term represents a phenomenological way to describe intraband transitions, which dominate at low energies. Since this term was not considered in our theory we will only compare our theoretical curves with experiment for energies larger than ~ 1 eV, since below this energy the Drude term is important whereas above it the intraband transitions are negligible. The calculated $\epsilon_2^\perp(\omega)$ in Fig. 1 has two pronounced peaks at ~ 4 and ~ 15 eV and a minimum at around ~ 9 eV. This should be compared with the experimental data, which also shows two peaks at ~ 4 and ~ 15 eV and a minimum around ~ 9 eV. Thus our calculations are in excellent agreement with experiment. In the high-energy regime (≥ 20 eV) both experiment and theory show a featureless behavior of $\epsilon_2^\perp(\omega)$.

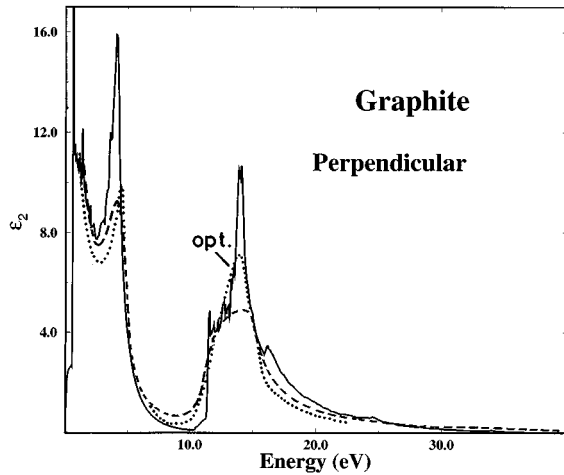


FIG. 1. Calculated and experimental ϵ_2^\perp of graphite. The solid line is the calculated ϵ_2^\perp while the dotted line (Ref. 30) and the dashed line (Refs. 31 and 29) are the experimentally measured ϵ_2^\perp .

The calculated $\epsilon_2^\parallel(\omega)$ in Fig. 2 also has two main features, one smaller at ~ 4 eV and a larger two peak feature at ~ 11 – 14 eV. In between these two peaks there is a minimum at around 9 eV. The experimental data are obtained from electron energy-loss spectra (EELS, dashed line) and from optical measurements (dotted line). It is somewhat disturbing that the two experimental curves are not consistent with each other and this makes a comparison with theory less straightforward. The optical measurements seem to resemble the theoretical two-peak structure at 11–14 eV, albeit with too low intensity. On the other hand, the EELS data have the correct intensity but show one dominating peak at 11 eV and a much weaker feature at 14 eV. We thus have to conclude that our theory does not fully agree with any of the two experimental curves. On the other hand one may question these experimental data, since they are not internally consistent. Further experimental efforts to resolve this problem are highly desired.

In order to analyze our calculated $\epsilon_2(\omega)$ curves we also calculated the joint density of states (JDOS); i.e., we evalu-

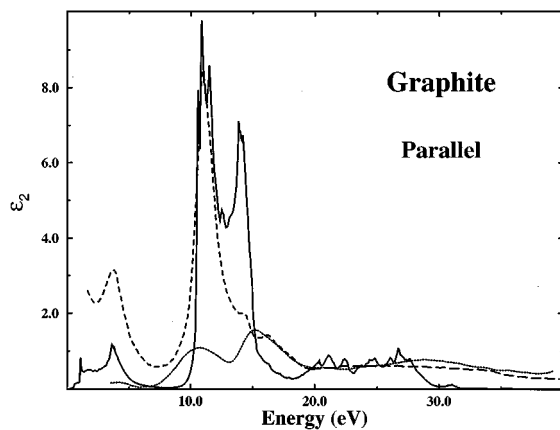


FIG. 2. Calculated and experimental ϵ_2^\parallel of graphite. The solid line is the calculated ϵ_2^\parallel while the dotted line (Ref. 32) is the experimental data deduced from optical measurements and the dashed line (Refs. 31 and 29) is obtained from electron energy-loss spectra.

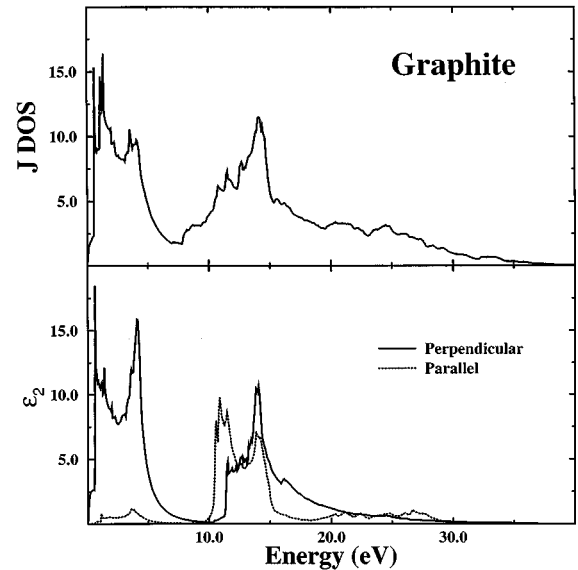


FIG. 3. Theoretical ϵ_2^\perp and ϵ_2^\parallel together with the joint density of states (JDOS) of graphite.

ated Eq. (2) setting all matrix elements equal to unity. The JDOS function is compared, in Fig. 3, with our calculated $\epsilon_2^\perp(\omega)$ and $\epsilon_2^\parallel(\omega)$ functions. Note that the JDOS curve shows some resemblance to the $\epsilon_2(\omega)$ functions. However, the inclusion of matrix elements shifts the relative intensities of certain peaks. This is especially pronounced for the features in the energy region 10–14 eV.

Next, we will try to explain the origin of the different peaks in the calculated dielectric functions. Since the different peaks are due to interband transitions it is useful for our discussion to first analyze the energy band structure. For this reason we display in Fig. 4 the calculated energy bands for graphite. In this figure we have also indicated which bands have σ , σ^* , π , and π^* character. Note that the in-plane σ orbitals give rise to low-lying bonding states in the energy range $\sim -20.0 \rightarrow -3.0$ eV and high-lying antibonding states in the energy range ~ 5.0 – 25.0 eV. The π bands, which are dominated by p_z orbitals, give rise to states in the energy region around the Fermi level (E_F). In an analysis of the

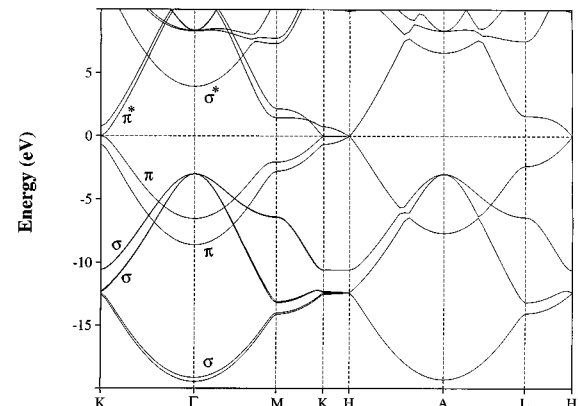


FIG. 4. Calculated energy band structure of graphite at the equilibrium volume along the major symmetry directions. Energy is in eV and the Fermi level (E_F) is set at zero energy.

optical transitions in graphite it is also important to consider the symmetry aspects of the different optical matrix elements, $\langle i|p_x|f\rangle$ and $\langle i|p_z|f\rangle$ (i and f are occupied and unoccupied band states, respectively), which enters Eq. (2). In order to do this it is illustrative to consider a simplified problem with only one isolated, single graphite layer. Since in bulk graphite the different atomic layers interact very little this is, from the electronic structure point of view, not a bad approximation. A single graphite plane has reflection symmetry in the plane and as a consequence the following symmetry restrictions apply to the matrix elements of the momentum operator: concerning p_x , transitions are only allowed from π to π^* or from σ to σ^* bands, and concerning p_z , transitions are only allowed from π to σ^* bands, or from σ to π^* bands. These requirements help to identify the different interband transitions that give rise to the dielectric function of graphite. An inspection of the different interband transitions (not shown) reveals that for $\epsilon_2^\perp(\omega)$ the features in the low-energy region (0 through ~ 5 eV) of Fig. 3 are mostly due to transitions between the π and π^* bands. From an inspection of the energy band structure (Fig. 4) this seems quite natural since on the line between M and K (a high symmetry line in the hexagonal plane of the Brillouin zone) the π and π^* bands show similar dispersion and are thus relatively parallel. Along this line these two bands are separated by 0 and ~ 5 eV and thus transitions between them give rise to peaks between 0 and ~ 5 eV. The features at ~ 14 eV of $\epsilon_2^\perp(\omega)$ mainly come from σ to σ^* states at points on the symmetry line between Γ and M . Concerning $\epsilon_2^\parallel(\omega)$ the absence of sharp features at low energies (0 through ~ 5 eV) may be understood from the fact that the only transitions that can give rise to such peaks are from π to π^* bands [in analogy with the discussion about the peak at ~ 4 eV for $\epsilon_2^\perp(\omega)$]. However, for p_z such transitions are forbidden for a single graphite layer. For the true three-dimensional lattice these transitions are not strictly forbidden but the matrix elements are much smaller than for p_x . This explains why there is a feature at ~ 4 eV in $\epsilon_2^\parallel(\omega)$ (Figs. 2 and 3), which is much smaller than the corresponding peak in $\epsilon_2^\perp(\omega)$. The peak at ~ 14 eV in $\epsilon_2^\parallel(\omega)$ is mainly due to transitions from π to σ^* at the points between K and Γ and between A and L as well as from transitions from σ to π^* at points between M and K , between H and A , and between A and L . The identification of the different interband transitions discussed above was made by a direct calculation of isolated band-band transitions in Eq. (2). In order to keep the length of our discussion within reasonable limits we have chosen not to display these individual transitions.

Having calculated $\epsilon_2(\omega)$, the function $\epsilon_1(\omega)$ is computed using the Kramers-Kronig transformation. This was done for both the parallel and perpendicular components. In Fig. 5 we compare experiment with theory for $\epsilon_1^\perp(\omega)$ and in Fig. 6 we compare our theoretical $\epsilon_1^\parallel(\omega)$ with the experimental data. Concerning $\epsilon_1^\perp(\omega)$ both experiment and our calculation show a feature with high intensity in the region 0–4 eV, a minimum at 5 eV and a peak at 14 eV. There is also a small minimum of $\epsilon_1^\perp(\omega)$ at 16 eV. The largest disagreement between theory and experiment is found at low energies ($\omega=0$). The reason for this is clear from an inspection of Eq. (11). In the limit $\omega \rightarrow 0$ the largest contribution to the

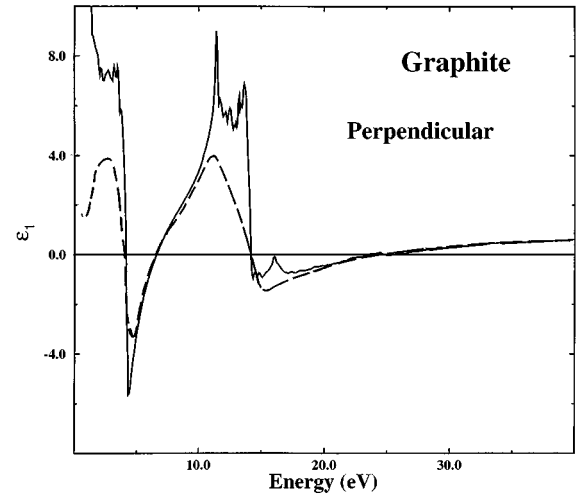


FIG. 5. Calculated and experimental ϵ_2^\perp of graphite. The solid line is the calculated ϵ_1^\perp while the dashed line (Refs. 31 and 29) is the experimentally measured ϵ_1^\perp .

integral comes from the energy region close to $\omega' = 0$. In this region the Drude term is important and since we have excluded this contribution the disagreement for ϵ_1 follows. For $\epsilon_1^\parallel(\omega)$ the experimental curve displays two peaks at around 3 and 11 eV and a minimum in between, at 5 eV. At ~ 12 eV there is, in the experimental data, a second, more pronounced minimum. Our calculations reproduce this behavior quite well except for the minimum at high energies, which occurs at slightly larger energies (15 eV) compared to experiment. For the same reason as for ϵ_1^\perp the neglect of a Drude term causes a large disagreement between experiment and theory in low-energy regime.

IV. CONCLUSIONS

We have described details of our implementation of calculations of the optical properties, $\epsilon_2(\omega)$ and $\epsilon_1(\omega)$, for the electric field component polarized both parallel and perpendicular to the crystallographic z axis, using a general potential electronic structure method, based on linear muffin-tin

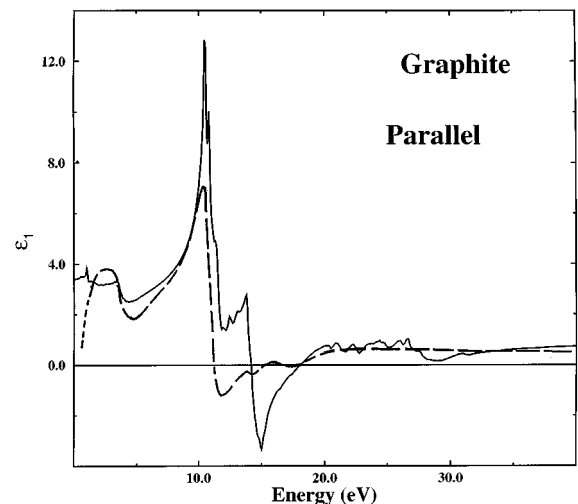


FIG. 6. Calculated and experimental ϵ_1^\parallel of graphite. The solid line is the calculated ϵ_1^\parallel while the dashed line (Refs. 31 and 29) is the experimentally measured ϵ_1^\parallel .

orbitals. With our method we have calculated the dielectric response of graphite, a highly anisotropic material. In the comparison with experimental data we have found quite good agreement for both the real and imaginary parts of the dielectric function. Apart from deviations from experiment in ϵ_1 at low energies (which we explain as due to the Drude contribution) the general shape of ϵ_2 and ϵ_1 is reproduced by our theory. This is quite encouraging especially since we base our theory on one-electron Kohn-Sham eigenvalues, which may quite easily be obtained for almost any system. Although it has not been proved that these eigenvalues actually correspond to quasiparticle excitations in a material, it has over the years been shown that the Kohn-Sham eigenvalues may to a good approximation be associated with excited-state properties, especially for optical data. We have also argued that due to symmetry considerations the perpen-

dicular component of $\epsilon_2(\omega)$ involves mostly $\pi \rightarrow \pi^*$ and $\sigma \rightarrow \sigma^*$ transitions and the parallel component of $\epsilon_2(\omega)$ involves mostly $\pi \rightarrow \sigma^*$ transitions and $\sigma \rightarrow \pi^*$ transitions. Such aspects of the interband transitions help identify the different bands and k points that are responsible for the optical transitions of graphite, and explains the unusually large anisotropy of the optical properties of graphite.

ACKNOWLEDGMENTS

We wish to thank the Swedish Natural Research Council and the Materials Consortium No. 9, sponsored by NUTEK and NFR, for financial support. Valuable discussions with Anna Delin and Jon Boettger are acknowledged. One of us (S.A.) would like to thank the Condensed Matter Theory Group at Uppsala University for their kind hospitality.

-
- ¹F. Tuinstra and J. L. Koenig, *J. Chem. Phys.* **53**, 1126 (1970).
²L. J. Brillson, E. Burstein, A. A. Maradudin, and T. Stark, in *Physics of Semimetals and Narrow Gap Semiconductors*, edited by D. L. Carter and R. T. Bate (Pergamon, New York, 1971), p. 187.
³R. J. Nemanich, G. Lucovsky, and S. A. Solin, in *Proceedings of the International Conference on Lattice Dynamics*, edited by M. Balkanski (Flammarion, Paris, 1975), p. 619.
⁴M. Hanfland, H. Beister, and K. Syassen, *Phys. Rev. B* **39**, 12 598 (1989).
⁵R. J. Nemanich, G. Lucovsky, and S. A. Solin, *Solid State Commun.* **23**, 117 (1977).
⁶M. Hanfland, K. Syassen, and R. Sonnenschein, *Phys. Rev. B* **40**, 1951 (1989).
⁷G. Bellodi, A. Borghesi, G. Guizzetti, L. Nosenzo, E. Reguzzoni, and G. Sammoggia, *Phys. Rev. B* **12**, 5951 (1975).
⁸R. Nicklow, N. Wakabayasi, and H. G. Smith, *Phys. Rev. B* **5**, 4951 (1977).
⁹O. L. Blaklee, D. G. Proctor, E. J. Seldin, G. B. Spence, and T. Wing, *J. Appl. Phys.* **41**, 3373 (1970); E. Seldin and C. W. Nezbeda, *ibid.* **41**, 3389 (1970).
¹⁰P. M. Williams, *Nuovo Cimento* **38B**, 216 (1977).
¹¹W. Eberhardt, I. T. McGovern, E. W. Plummer, and J. E. Fisher, *Phys. Rev. Lett.* **21**, 200 (1980).
¹²A. R. Law, J. J. Bary, and H. P. Hughes, *Phys. Rev. B* **28**, 5332 (1983).
¹³T. Takahashi, H. Tokailin, and T. Sagawa, *Phys. Rev. B* **32**, 8317 (1985).
¹⁴V. Dose, G. Reusing, and H. Scheidt, *Phys. Rev. B* **26**, 984 (1982).
¹⁵D. Marchand, C. Frétygny, M. Laguës, F. Batallain, Ch. Simon, I. Rosenman, and R. Pinchaux, *Phys. Rev. B* **30**, 4788 (1984).
¹⁶R. Claessen, H. Cartensen, and M. Skibowski, *Phys. Rev. B* **38**, 12 582 (1988).
¹⁷I. R. Collins, P. T. Andrews, and A. R. Law, *Phys. Rev. B* **38**, 13 348 (1988).
¹⁸F. Maeda, T. Takahashi, H. Ohsawa, S. Suzuki, and H. Suematsu, *Phys. Rev. B* **37**, 4482 (1988).
¹⁹J. W. McClure, *Phys. Rev.* **108**, 612 (1957).
²⁰J. C. Slonczewski and P. R. Weiss, *Phys. Rev.* **109**, 272 (1958).
²¹A. Zunger, *Phys. Rev. B* **17**, 626 (1978).
²²R. C. Tatar and S. Rabii, *Phys. Rev. B* **25**, 4126 (1982).
²³H. J. F. Jansen and A. J. Freeman, *Phys. Rev. B* **35**, 8207 (1987).
²⁴D. A. Fisher, R. M. Wentzcovitch, R. G. Carr, A. Continenza, and A. J. Freeman, *Phys. Rev. B* **44**, 1427 (1991).
²⁵N. A. W. Holzwarth, S. G. Louie, and S. Rabii, *Phys. Rev. B* **26**, 5382 (1982).
²⁶J.-C. Charlier, X. Gonze, and J.-P. Michenaud, *Phys. Rev. B* **43**, 4579 (1991).
²⁷M. C. Schabel and J. L. Martins, *Phys. Rev. B* **46**, 7185 (1992).
²⁸R. Ahuja, S. Auluck, J. Trygg, O. Eriksson, J. M. Wills, and B. Johansson, *Phys. Rev. B* **51**, 4813 (1995).
²⁹J. Daniels, C. von Festenberg, H. Raether, and K. Zeppenfeld, *Optical Constants of Solids by Electron Spectroscopy*, in Springer Tracts in Modern Physics Vol. 54 (Springer, Berlin, 1970), pp. 126–130.
³⁰E. A. Taft and H. R. Philipp, *Phys. Rev.* **138**, A197 (1965).
³¹K. Zeppenfeld, thesis, Universität Hamburg, 1969.
³²R. Klucker, M. Skibowski, and W. Steinmann, *Phys. Status Solidi B* **65**, 703 (1974).
³³J. R. Anderson, W. J. O'Sullivan, J. E. Schirber, and D. E. Soule, *Phys. Rev.* **164**, 1038 (1967).
³⁴J. M. Wills (unpublished); J. M. Wills and B. R. Cooper, *Phys. Rev. B* **36**, 3809 (1987); D. L. Price and B. R. Cooper, *ibid.* **39**, 4945 (1989).
³⁵O. K. Andersen, *Phys. Rev. B* **12**, 3060 (1975).
³⁶H. L. Skriver, *The LMTO Method* (Springer, Berlin, 1984).
³⁷D. J. Chadi and M. L. Cohen, *Phys. Rev. B* **8**, 5747 (1973); S. Froyen, *ibid.* **39**, 3168 (1989).
³⁸L. Hedin and B. I. Lundqvist, *J. Phys. C* **4**, 2064 (1971).
³⁹A good description of the calculation of dielectric constants and related properties are found in the thesis by T. Gasche, Uppsala University, 1993.
⁴⁰A. R. Edmonds, *Angular Momentum in Quantum Mechanics* (Princeton University Press, Princeton, 1974), p. 82.
⁴¹In practice we calculate matrix elements of the symmetrized momentum operator $\langle i | \vec{p}_{\mu} | j \rangle \equiv [\langle i | p_{\mu} | j \rangle + (-1)^{\mu} \langle p_{-\mu} | i | j \rangle] / 2$.
⁴²P. M. Oppeneer, T. Maurer, J. Sticht, and J. Kübler, *Phys. Rev. B* **45**, 10 924 (1992).
⁴³O. K. Andersen and R. V. Kasowski, *Phys. Rev. B* **4**, 1064 (1971).
⁴⁴A. Bianconi, S. B. M. Hagström, and R. Z. Bachkrach, *Phys. Rev. B* **16**, 5543 (1977).